PNAS PLUS

Kinetic isotope effects reveal early transition state of protein lysine methyltransferase SET8

Joshua A. Linscott[a,b,1], Kanishk Kapilashrami[a,1], Zhen Wang[c], Chamara Senevirathne[a], Ian R. Bothwell[a,d], Gil Blum[a,d], and Minkui Luo[a,b,2]

[a]Chemical Biology Program, Memorial Sloan Kettering Cancer Center, New York, NY 10065; [b]Program of Pharmacology, Weill Graduate School of Medical Science, Cornell University, New York, NY 10021; [c]Department of Biochemistry, Albert Einstein College of Medicine, Bronx, NY 10461; and [d]Tri-Institutional PhD Program in Chemical Biology, Memorial Sloan Kettering Cancer Center, New York, NY 10065

Edited by Frank M. Raushel, Texas A&M University, College Station, TX, and accepted by Editorial Board Member Michael A. Marletta November 9, 2016 (received for review June 4, 2016)

Protein lysine methyltransferases (PKMTs) catalyze the methylation of protein substrates, and their dysregulation has been linked to many diseases, including cancer. Accumulated evidence suggests that the reaction path of PKMT-catalyzed methylation consists of the formation of a cofactor(cosubstrate)–PKMT–substrate complex, lysine deprotonation through dynamic water channels, and a nucleophilic substitution (S_N2) transition state for transmethylation. However, the molecular characters of the proposed process remain to be elucidated experimentally. Here we developed a matrix-assisted laser desorption ionization time-of-flight mass spectrometry (MALDI-TOF-MS) method and corresponding mathematic matrix to determine precisely the ratios of isotopically methylated peptides. This approach may be generally applicable for examining the kinetic isotope effects (KIEs) of posttranslational modifying enzymes. Protein lysine methyltransferase SET8 is the sole PKMT to monomethylate histone 4 lysine 20 (H4K20) and its function has been implicated in normal cell cycle progression and cancer metastasis. We therefore implemented the MS-based method to measure KIEs and binding isotope effects (BIEs) of the cofactor *S*-adenosyl-L-methionine (SAM) for SET8-catalyzed H4K20 monomethylation. A primary intrinsic ^{13}C KIE of 1.04, an inverse intrinsic α-secondary CD_3 KIE of 0.90, and a small but statistically significant inverse CD_3 BIE of 0.96, in combination with computational modeling, revealed that SET8-catalyzed methylation proceeds through an early, asymmetrical S_N2 transition state with the C-N and C-S distances of 2.35–2.40 Å and 2.00–2.05 Å, respectively. This transition state is further supported by the KIEs, BIEs, and steady-state kinetics with the SAM analog *Se*-adenosyl-L-selenomethionine (SeAM) as a cofactor surrogate. The distinct transition states between protein methyltransferases present the opportunity to design selective transition-state analog inhibitors.

PMT | PKMT | KIE | BIE | methylation

Stepwise progression of an enzyme-catalyzed chemical reaction is accompanied by changes of bond orders and vibrational modes involved with specific atoms of the reactant(s) (1, 2). Such changes can be traced experimentally by measuring the ratios of turnover rates [kinetic isotope effects (KIEs)] or binding affinities [binding isotope effects (BIEs)] of the reactant(s) when the relevant atoms are replaced by heavy isotopes (3, 4). KIEs and BIEs are thus useful parameters for elucidating transition-state (TS) structures and catalytic mechanisms, which sometimes cannot be elucidated readily through sole measurement of steady-state kinetics (5–9). A sufficient set of KIEs and BIEs at the positions involved with bond motions can afford electrostatic and geometric constraints, when combined with computational modeling, to define an enzymatic TS (10–12). This information provides not only the atomic resolution of the transient structure at the highest energy summit along the reaction path, but also structural guidance for designing tight-binding TS analog inhibitors (13, 14).

Multiple approaches have been documented to measure KIEs and BIEs of enzymatic reactions (3, 15–17). A conventional method is to determine individual steady-state kinetic parameters (k_{cat} and K_m) with a pair of isotopic substrates and then calculate their ratios (18). This method is straightforward and can afford kinetic parameters and thus noncompetitive KIEs beyond ±10% from unity (2). Given that the values of many KIEs and BIEs of enzymatic reactions are within a range of a few percent from unity, more precise measurement requires enzymatic reactions to be carried out competitively with mixed isotopic substrates. This competitive condition is expected to minimize the errors originating from sample-to-sample variation (19, 20). The isotopic ratios of prereacted substrates vs. bound substrates or depleted substrates (or unconsumed substrates) are then quantified for the calculation of BIEs or KIEs, respectively. Several approaches that can precisely determine isotopic ratios of two mixed isomers are remote radioactive labeling, 1D/2D NMR spectroscopy, and isotope ratio MS (16, 21–23).

Protein lysine methyltransferases (PKMTs) belong to a subfamily of posttranslational modifying enzymes (24, 25). PKMTs catalyze the methylation of histone and nonhistone protein substrates at targeted lysine residues (26–28). All PKMTs use *S*-adenosyl-L-methionine (SAM) as a ubiquitous methyl donor (cosubstrate or cofactor with the latter used thereafter), but diverge in terms of their degree of substrate methylation (mono-, di-, and tri-) (29). PKMTs can play essential roles in modulating

Significance

We developed an MS-based method to determine kinetic isotope effects and binding isotope effects on protein lysine methyltransferase SET8-catalyzed monomethylation. These parameters, coupled with steady-state kinetics and molecular modeling, outlined the reaction path of SET8-catalyzed methylation. Upon the formation of the *S*-adenosyl-L-methionine–SET8–histone 4 lysine 20 intermediate complex followed by lysine deprotonation, the reaction goes through an early, asymmetrical transition state (TS) with the small engagement of the C-N bond and the partial dissociation of the C-S bond. This TS structure is distinct from the known TS structures of other protein lysine methyltransferases (PKMTs) and thus presents the feasibility to design selective TS analog inhibitors against PKMTs. The developed techniques can also be generally applicable to examining other protein methylation and posttranslational modifications.

Author contributions: J.A.L., K.K., Z.W., and M.L. designed research; J.A.L., K.K., Z.W., and G.B. performed research; J.A.L., K.K., C.S., I.R.B., and G.B. contributed new reagents/analytic tools; J.A.L., K.K., Z.W., and M.L. analyzed data; and J.A.L., K.K., Z.W., and M.L. wrote the paper.

The authors declare no conflict of interest.

This article is a PNAS Direct Submission. F.M.R. is a Guest Editor invited by the Editorial Board.

[1]J.A.L. and K.K. contributed equally to this work.

[2]To whom correspondence should be addressed. Email: luom@mskcc.org.

This article contains supporting information online at www.pnas.org/lookup/suppl/doi:10.1073/pnas.1609032114/-/DCSupplemental.

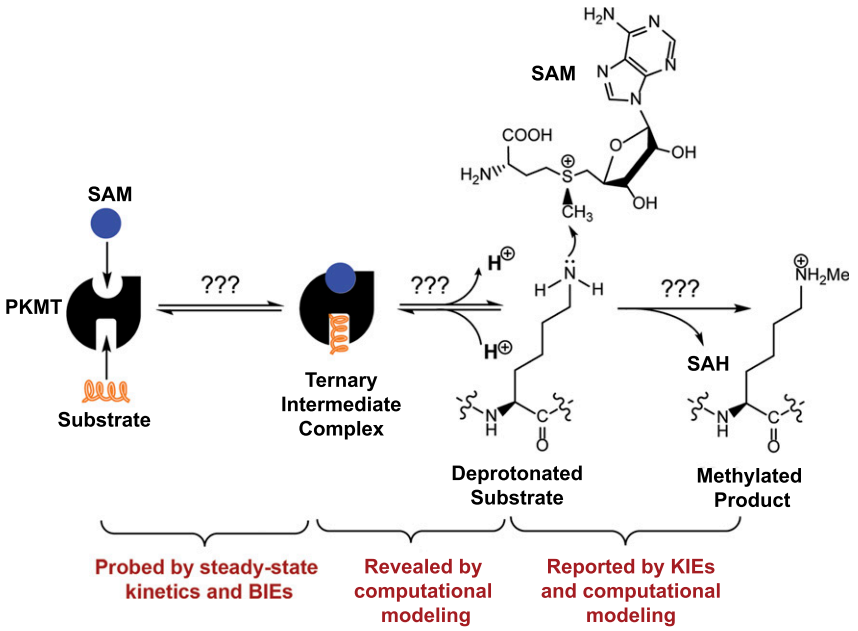

Fig. 1. A hypothetical reaction path of PKMT-catalyzed lysine monomethylation and relevant biochemical methods to examine each aspect of the process.

gene transcription, cellular differentiation, and organ development, and their dysregulation has been frequently implicated in diseases, including cancer (26, 30, 31). Most PKMTs are characterized by their canonical ∼130-aa SET domain (>50 aa encoded by the human genome) (24, 25). Several PKMTs have been examined previously under steady-state conditions and shown to follow a bisubstrate random or ordered sequential mechanism to bind SAM and substrates (Fig. 1) (32, 33). Computational modeling suggests that the target lysine residues of substrates are subject to deprotonation through dynamic water channels, followed by a putative nucleophilic substitution (S_N2) TS for the transmethylation reaction (Fig. 1) (34, 35). However, limited efforts have been made to explore experimentally the (S_N2) TS of PKMT-catalyzed methylation. Recent evidence from static PKMT structures and dynamic NMR chemical shifts suggests the existence of equatorial noncanonical CH–O interaction between the sulfonium methyl moiety of SAM and the oxygens of active-site amino acid residues of PKMTs (36–38), although it remains to examine how the equatorial CH–O interaction participates in the formation of the TS of PKMT-catalyzed methylation reaction.

Protein lysine methyltransferase SET8 is the sole PKMT to monomethylate histone 4 lysine 20 (H4K20) and its functions have been implicated for normal cell cycle progression and cancer metastasis (39–41). The biological relevance of SET8, as well as our general interest in PKMTs, inspired us to leverage BIE and KIE studies of SET8 to explore bond motions along the reaction path of the PKMT-catalyzed methylation. Given the convenience of MS in characterizing protein methylation (42, 43), we developed a matrix-assisted laser desorption ionization time-of-flight mass spectrometry (MALDI-TOF-MS) method and corresponding mathematic matrix to determine precisely the ratios of isotopically labeled H4K20 peptide. With this approach, BIEs and KIEs of SAM and SeAM (*Se*-adenosyl-L-selenomethionine, a more reactive SAM surrogate) were determined for SET8-catalzyed H4K20 methylation. An inverse α-secondary (α-2°-CD_3) CD_3 KIE and a normal primary ^{13}C KIE (1°-^{13}C KIE) of SAM, together with computational modeling, indicate that SET8 adapts an early, asymmetrical S_N2 TS for H4K20 methylation. In contrast, a small inverse BIE of [*S*-CD_3]-SAM, together with structural evidence, argues that the large inverse intrinsic CD_3 KIE originates from the structural changes at the TS rather than upon the formation of the SAM–SET8 complex. The small inverse BIE of [*S*-CD_3]-SAM could arise from the noncanonical CH–O interaction upon the formation of the SAM–SET8 complex. These results are also consistent with BIE and steady-state kinetics of SeAM as a cofactor surrogate. Collectively, the characteristic KIEs and BIEs, together with structural and computational evidence, delineate the TS of SET8-catalyzed H4K20 monomethylation. The current work further serves as a starting point to leverage the MALDI-TOF-MS method to measure KIEs and BIEs of other PKMTs for characterizing their TS structures. Knowing the differences between these TS structures can be a key step toward developing selective TS analog inhibitors.

Results and Discussion

Kinetics of SET8-Catalyzed H4K20 Monomethylation. To use SET8-catalyzed H4K20 monomethylation as a model for studying KIEs and dissecting reaction paths of PKMTs, we first examined steady-state kinetics of SET8 with the SAM cofactor and H4K20 peptide substrate (Fig. S1). We previously developed an enzyme-coupled luciferase assay for PKMTs and demonstrated its use to characterize the steady-state kinetics of SET7/9 (44). In the assay, the reaction progress was monitored with a luciferin–luciferase kit by converting enzymatically the reaction byproduct *S*-adenosyl-L-homocysteine (SAH) into ATP. This assay was implemented to characterize the steady-state kinetics of SET8-catalyzed H4K20 methylation. By systematically altering the concentrations of the SAM cofactor and H4K20 peptide substrate, the initial velocities of SET8-catalyzed methylation were obtained by plotting the initial linear increase of luminescence vs. reaction time (10–20 min, depending on the concentrations of SAM and H4K20 peptide) (Fig. S1*A*). The initial velocities were then plotted against the concentrations of SAM and H4K20 to generate double-reciprocal curves (Fig. S1 *B* and *C*) (44, 45). Here, the linear regression converged in the second quadrant rather than on the *y* axis and thus excluded a ping-pong mechanism and a rapid-equilibrium ordered sequential mechanism (46). Because four possible mechanisms (rapid-equilibrium random, steady-state random, steady-state ordered, and Theorell–Chance) can fit the current kinetic data and dissecting the exact

Table 1. Comparison of apparent steady-state kinetics (k_{cat} and K_m), BIEs, forward commitment factors, KIEs, and BIEs with SAM and SeAM as cofactors (cosubstrates) in SET8-catalyzed H4K20 monomethylation

Parameters	SAM	SeAM
k_{cat}, min^{-1}	7.0 ± 0.8	13 ± 2*
K_m, μM	16 ± 6	16 ± 6*
CD_3 or $^{13}CD_3$ BIE	0.959 ± 0.006	0.962 ± 0.004
CT_3 or $^{14}CT_3$ BIE	0.979 ± 0.009	NA
C_f	0.10 ± 0.01	0.10 ± 0.01
$^{CD_3}(V/K)$	0.878 ± 0.008	0.99 ± 0.02
^{CD_3}k	0.90 ± 0.01	1.02 ± 0.02
^{CD_3}k, calculated	0.896†	1.018‡
$^{13CD_3}(V/K)$	0.907 ± 0.007	1.04 ± 0.01
$^{13CD_3}k$	0.94 ± 0.02	1.09 ± 0.02
$^{13CH_3}k$	1.04 ± 0.02	1.06 ± 0.02
$^{13CH_3}k$, calculated	1.058†	1.061‡
$^{CT_3/14CH_3}(V/K)$	0.785 ± 0.009	NA
$^{CT_3/14CH_3}k$	0.78 ± 0.01	NA
$^{CT_3/14CH_3}k$, calculated	0.773†	NA

NA, not applicable.

*These values were calculated on the basis of k_{cat} and K_m values of SAM, $^{SeAM/SAM}(k_{cat}/K_{m,cofactor})$ and $^{SeAM/SAM}(1/K_{m,cofactor})$ (1.94 and 1.03 for the latter two, respectively).

†The experimental SAM KIEs match TS structures with $d_{C\text{-}S}$ = 2.00–2.05 Å and $d_{C\text{-}N}$ = 2.35–2.40 Å. The calculated KIEs are listed for a representative TS structure with $d_{C\text{-}S}$ = 2.05 Å (bond order 0.845), and $d_{C\text{-}N}$ = 2.38 Å (bond order 0.117).

‡The experimental SeAM KIEs match a wide range of TS structures with $d_{C\text{-}Se}$ + $d_{C\text{-}N}$ = 4.8–4.9 Å. The calculated KIEs are listed for a representative TS structure with $d_{C\text{-}Se}$ = 2.50 Å and $d_{C\text{-}N}$ = 2.35 Å.

kinetic mechanism is not the focus of this work, we globally fitted the experimental data, using Eqs. **S1** and **S2** (*SI Materials and Methods*). The enzymatic turnover k_{cat} of 7.0 ± 0.8 min^{-1}, $K_{m,SAM}$ of 16 ± 6 μM, $K_{m,H4K20}$ of 40 ± 8 μM, and α of 1.4 were obtained (Fig. S1*D* and Table 1).

Quantification of Isotopic Ratios by Deconvoluted MALDI-TOF MS. Whereas several previously established methods show capability for precise measurement of KIEs, MALDI-TOF MS was implemented here because of the generality and convenience of this method to probe protein posttranslational modifications with isotopically labeled cofactors (2, 3, 15, 21, 47). Unmodified H4K20 peptide displays a dominant characteristic set of six mass multiplets, which maintain fixed ratios of individual peak areas and arise from natural isotope abundance of ^{13}C and other heteroatoms (Figs. 2*A*, 3, and 4). Modifying this peptide by one equivalent of [*S*-CH_3]-SAM or [*S*-CD_3]-SAM causes +14-Da ($^{CH_3}Area_{1-6}$) or +17-Da ($^{CD_3}Area_{4-9}$) mass shifts, respectively, without causing a significant change of the peak ratios among the six multiplets (Figs. 3*A* and 4*A*). Modification of H4K20 peptide by a mixture of [*S*-CH_3]-SAM and [*S*-CD_3]-SAM results in nine mass multiplets, of which the first three peaks ($^{CH_3}Area_i$, i = 1,2,3) and the last three peaks ($^{CD_3}Area_i$, i = 7,8,9) arise from [*S*-CH_3]-SAM and [*S*-CD_3]-SAM, respectively (Fig. 3*A*). The three central peaks ($^{CH_3+CD_3}Area_j$, j = 4,5,6) are the sum of the overlapping modification by both [*S*-CH_3]-SAM and [*S*-CD_3]-SAM. Given the fixed ratios for individual sets of six multiplets, the contribution of [*S*-CH_3]-SAM ($^{CH_3}Area_j$) and [*S*-CD_3]-SAM ($^{CD_3}Area_j$) to their sum ($^{CH_3+CD_3}Area_j$, j = 4,5,6) was deconvoluted with either the first three ($^{CH_3}Area_i$, i = 1,2,3) or the last three ($^{CD_3}Area_i$, i = 7,8,9) nonoverlapping peaks as independent variables (*SI Materials and Methods*). The resulting two sets of peak areas $^{CH_3(CD_3)}Area_{j,1}$ and $^{CH_3(CD_3)}Area_{j,2}$ were then averaged according to their relative weights ($\sum_{i=1}^{3} {}^{CH_3}Area_i$ vs. $\sum_{i=7}^{9} {}^{CD_3}Area_i$) (Fig. 3*A*). Similarly, modifying the H4K20 peptide by one equivalent of [*S*-CH_3]-SAM or [*S*-$^{13}CD_3$]-SAM causes +14-Da ($^{CH_3}Area_{1-6}$) or +18-Da ($^{^{13}CD_3}Area_{5-10}$) mass shift, respectively (Figs. 3*B* and 4*B*). The resultant isotopic ratios can be deconvoluted in a similar manner (*SI Materials and Methods*). The robustness of our MS-based deconvolution method to distinguish small changes of isotopic ratios was validated by its reproducible readouts (100% ± 0.3% precision) with isotopically modified peptides (Table 1) and the consistence of the resultant BIEs and KIEs with those obtained with the conventional radiometric method (see BIE and KIE of the [*S*-CT_3]/[*S*-$^{14}CH_3$]-SAM cofactor pair). The MS-based deconvolution method was thus implemented in the current work to examine CD_3 BIE, CD_3 KIE, and $^{13}CD_3$ KIE of SET8-catalyzed H4K20 monomethylation. This MS-based method is expected to be generally applicable to examining BIEs and KIEs of PKMTs as well as other posttranslational modifications.

Inverse BIEs of [*S*-CD_3]-SAM and [*S*-CT_3]-SAM. Several prior works have shown that significant KIEs can arise from BIEs during the formation of a substrate–enzyme complex rather than the bond-order or conformational changes at the enzymatic TS (6, 48). The BIEs can either positively or negatively affect observed KIEs (49). Before obtaining ^{CD_3}k, we therefore evaluated the potential contribution of the BIE of [*S*-CD_3]-SAM along the path of the SET8-catalyzed methylation reaction (Fig. 2*B*). A small but significant inverse CD_3 BIE of 0.959 ± 0.006 was obtained upon calculating the difference of the isotopic ratios between pre-bound and SET8-bound SAM cofactors (Table 1). Given the small magnitude of the inverse CD_3 BIE revealed by the MS-based method, we further validated the approach and the resultant inverse CT_3 BIE with a radiometric method, using the [*S*-CT_3]/[*S*-$^{14}CH_3$]-SAM cofactor pair. Both [*S*-CD_3]-SAM and [*S*-CT_3]-SAM show small but significantly inverse BIEs (Table 1). These results indicate an increased vibrational stiffness of the sulfonium-methyl group of SAM upon its binding by SET8.

Inverse α-2°-CD_3 KIE for SET8-Catalyzed H4K20 Methylation with [*S*-CD_3]-SAM as Cofactor. The three hydrogen atoms of the sulfonium methyl group of SAM are one bond away from the electrophilic sulfonium-methyl reaction center. $^{CD_3}(V/K)$ of [*S*-CD_3]-SAM is expected to reflect the accumulated changes of bond orders and vibration modes involved with the deuterium atoms of the SAM cofactor from its unbound ground state to the enzymatic TS (1). Given the ability of the MS deconvolution method to distinguish the small changes of the isotopic ratios of the modified peptide product, we carried out internal competition experiments with a mixture of [*S*-CH_3]-SAM and [*S*-CD_3]-SAM cofactors and measured the α-2°-CD_3 KIE of SET8-catalyzed H4K20 methylation (Figs. 3*A* and 4*A*). In these experiments, [*S*-CD_3]-SAM displayed $^{CD_3}(V/K)$ of 0.878 ± 0.008 (Table 1). In comparison with the intrinsic α-2°-CD_3 KIE, the $^{CD_3}(V/K)$ obtained above under the competitive conditions could be suppressed by forward commitment factor (C_f) and reverse commitment factor (C_r), respectively (19). We then measured the C_f of the cofactor in SET8-catalyzed H4K20 methylation with an isotope-trapping method (*SI Materials and Methods*). SET8 displays a small C_f (10%) for SAM cofactor (Table 1), suggesting that SAM is subject to a rapid exchange between its unbound and SET8-bound form within the timescale of the progression of the SET8-bound SAM toward the reaction product. The C_r of SET8 for SAM is negligible because of the formation of the stronger N-C bond and thus the irreversible character of SET8-catalyzed methylation reaction. Upon correction for C_f and BIE (*Materials and Methods*, Eqs. **1**, **2a**, and **2b**), ^{CD_3}k of 0.90 ± 0.01 of [*S*-CD_3]-SAM was obtained for SET8-catalyzed methylation (Table 1). The significantly inverse α-2 °CD_3 KIE of around 10%, together with the small inverse CD_3 BIE of around 4% (Table 1), argues that that the vibrational stiffness of the sulfonium-methyl group

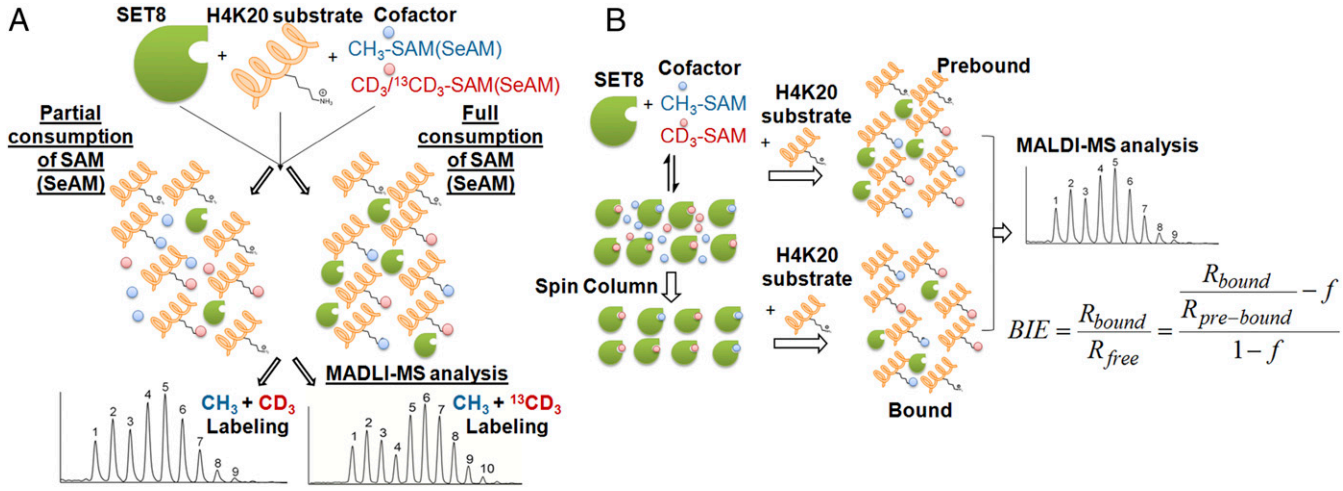

Fig. 2. Overview of KIE measurement under competitive conditions. (*A*) Schematic description of a competition reaction with a pair of isotopic cofactors and the resultant overlapping MS data with CH_3/CD_3 and $CH_3/^{13}CD_3$ cofactor pairs. The reaction sample was split into two portions for partial consumption and full consumption of the pair of isotopic cofactors, respectively. Their light-to-heavy isotope ratios (blue vs. red) are quantified by MS as described in *Materials and Methods*. (*B*) Schematic description of BIE measurement under competitive conditions. Here a pair of prebound or SET8-bound CH_3/CD_3 isotopic cofactors were converted to label H4K20 peptide substrate under competitive conditions. The resultant methylated H4K20 peptide was subjected to MS analysis to quantify the isotopic ratios as described in *Materials and Methods*.

of SAM is subject to a small increase upon the formation of the SAM–SET8 binary complex (a modest inverse BIE of 0.96) and then a more dramatic increase along the reaction path toward its TS (a significant inverse intrinsic α-2°-CD_3 KIE of 0.90) (Table 1).

Normal 1°-^{13}C KIE for SET8-Catalyzed H4K20 Methylation. Because the magnitude of ${}^{CD_3}k$ is sensitive to many factors besides the change of bond orders at the TS, we determined the intrinsic 1°-^{13}C KIE (${}^{13CH_3}k$) as another constraint to uncover the TS of SET8-catalyzed H4K20 methylation. Here ${}^{13CD_3}(V/K)$ and ${}^{13CD_3}k$ were obtained similarly with the MS-based method with [*S*-CH_3]-SAM and [*S*-$^{13}CD_3$]-SAM as a cofactor pair (Figs. 3*B* and 4*B*). Here the use of [*S*-CH_3]-SAM paired with [*S*-$^{13}CD_3$]-SAM rather than [*S*-$^{13}CH_3$]-SAM is expected to give better separation and thus precise isotopic quantification of the MALDI multiples of the products. The intrinsic 1°-^{13}C KIE was obtained after correcting ${}^{CD_3}k$ from ${}^{13CD_3}k$ according to ${}^{13CD_3}k = {}^{13CH_3}k \cdot {}^{CD_3}k$. Based on the rule of the geometric mean (50), the free energy contributions from two-isotope labeling in a molecule are additive; thus, the dual-labeling intrinsic KIE is the product of individual intrinsic KIEs; e.g., ${}^{13CD_3}k = {}^{13CH_3}k \cdot {}^{CD_3}k$. It is important to point out that the rule of geometric mean generally holds very well except in some hydrogen transfer reactions involving significant quantum-mechanic (QM) tunneling effects (51). The normal primary ${}^{13CH_3}k$ of 1.04 ± 0.02 indicates that there is a small decrease of the overall bond order of the methyl carbon of SAM from the SET8-bound ground state to the enzymatic TS (Table 1).

Computational Modeling of Transition State of SET8-Catalyzed H4K20 Methylation. Molecular dynamic simulation suggested that SET8 catalyzes H4K20 monomethylation through an early S_N2 TS with the C-N distance of 2.46 ± 0.15 Å, the C-S bond distance of 2.01 ± 0.12 Å, and the N-C-S bond angle of 172° (34). This coordinate is also in agreement with the C-S distance extracted from the crystal structure of the ternary complex of SET8 with the reaction products SAH and H4K20me (PDB ID: 2BQZ). Starting from the atomic coordinates of the SAH-SET8-H4K20me complex, we gradually altered the C-N and C-S distances (*Materials and Methods*) to search for the TS candidates with the experimental KIEs as geometrical constraints (${}^{CD_3}k = 0.90 \pm 0.01$ and ${}^{13CH_3}k = 1.04 \pm 0.02$). Geometry optimizations and frequency calculations were performed by Gaussian09 (52) with a density functional theory with an M062X functional and 6-31+G(d,p) basis set (53), and KIEs were calculated using ISOEFF (54). The only TS geometry that matches the experimental KIEs shows early, asymmetrical S_N2 TS characters with the C-N distance of 2.35–2.40 Å (bond order ~0.12) and the C-S bond distance of 2.00–2.05 Å (bond order ~0.85, Table 1 and Fig. 5). The modestly inverse ${}^{CD_3}k$ of 0.90 is a key parameter to define the distinct TS geometry because late, asymmetrical S_N2 TS geometries, although with the matched ${}^{13CH_3}k$ of 1.04, were calculated to show a higher magnitude of inverse ${}^{CD_3}k$ (${}^{CD_3}k < 0.7$). The TS uncovered by KIEs is in remarkable agreement with the TS structure proposed by molecular dynamics simulations (2.35–2.40 Å vs. 2.46 ± 0.15 Å for C-N distances; 2.00–2.05 Å vs. 2.01 ± 0.12 for C-S distances). In contrast, the TS geometry without KIE constraints showed nearly symmetric characters with the C-N distance of 2.1 Å (bond order ~0.32) and the C-S bond distance of 2.2 Å (bond order ~0.62). These results delineated that SETD8 catalyzes the H4K20 monomethylation through an early, asymmetrical S_N2 TS with the N-C distance around 2.4 Å, the N-S distance of 4.4 Å, and the N-C-S bond angle of 178° (Fig. 5). This KIE-constrained TS is enzymatically facilitated and is distinct from the TS obtained upon relaxing the C-N and C-S distances.

Additional Confirmation of Transition State of SET8-Catalyzed H4K20 Methylation Using ${}^{CT_3/14CH_3}k$. To validate the accuracy of KIEs obtained by the MALDI-TOF-MS method, we determined ${}^{CT_3/14CH_3}k$ with the [*S*-CT_3]-SAM and [*S*-$^{14}CH_3$]-SAM as the paired cofactors, using an established radiometric method. The ${}^{CT_3/14CH_3}k$ of 0.78 ± 0.01 is in agreement with the theoretical ${}^{CT_3/14CH_3}k = 0.773$ obtained for the TS structure with the MS-based KIEs as experimental constraints (Table 1). Such consistency further validates the accuracy of the MALDI-TOF-MS method to determine KIEs as well as the KIE-constrained TS structure.

Origins of KIEs and Their Implication for an S_N2 Transition State of SET8-Catalyzed Methylation with SAM as a Cofactor. The large inverse ${}^{CD_3}(V/K)$ of 0.878 and ${}^{CD_3}k$ of 0.90 for [*S*-CD_3]-SAM for the SET8-catalyzed methylation argues for a more constrained

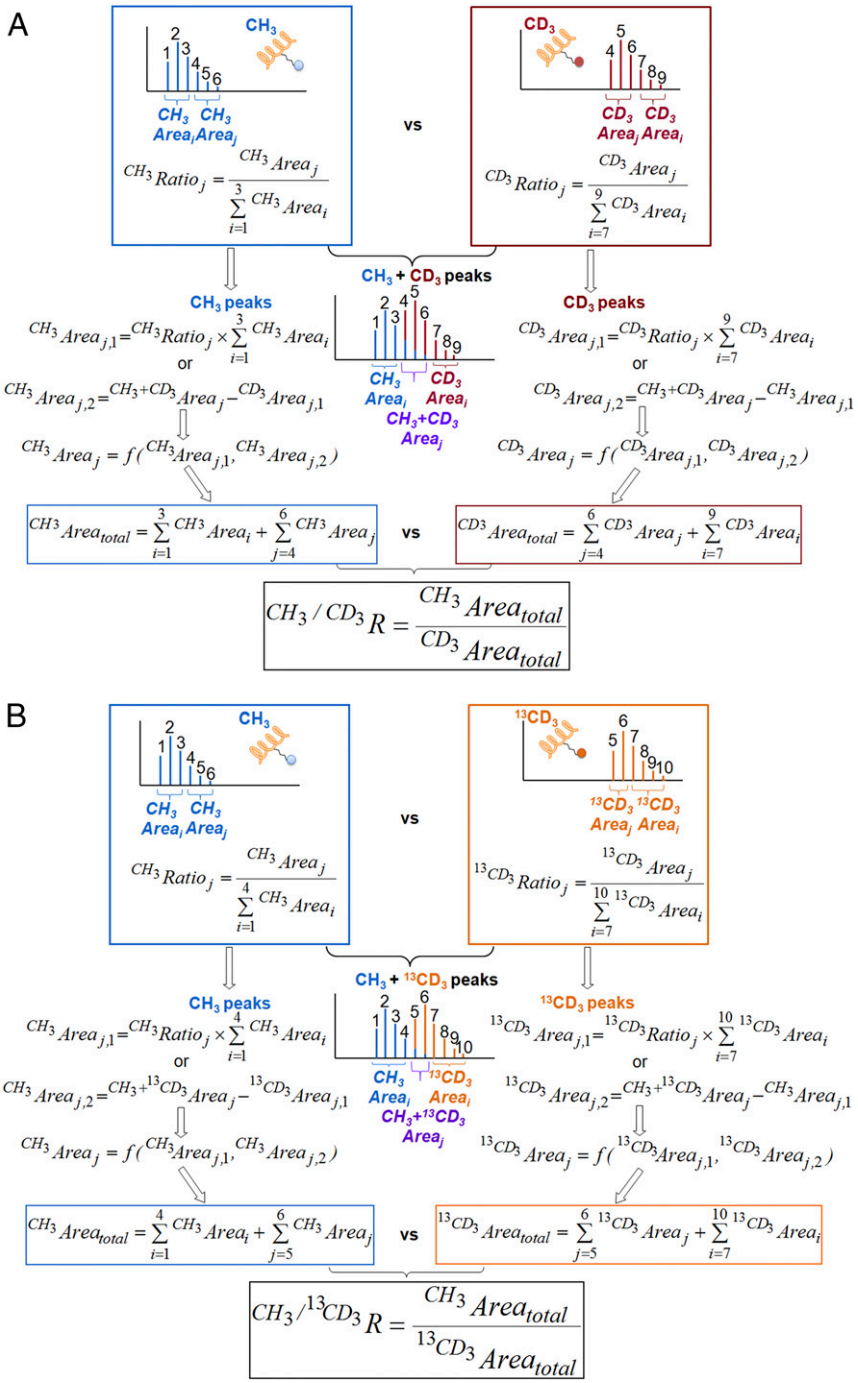

Fig. 3. Overview of mathematical matrix to deconvolute the MS data and calculate light-to-heavy isotope ratios according to Eqs. S3–S7. (*A*) -CH_3 vs. -CD_3 (blue vs. red) (*B*) -CH_3 vs. -$^{13}CD_3$ (blue vs. orange).

TS around the methyl group of SAM in comparison with its unbound and SET8-bound ground states. A significant inverse CD_3 BIE of 0.959 suggests that the binding of SAM to SET8 is accompanied by a certain degree of the stiffness of the methyl group of SAM. Along the reaction path, the stiffness of the methyl group is further enhanced from SET8-bound SAM to the TS as reflected by a larger inverse ^{CD_3}k of 0.90. Several previous studies have reported inverse CD_3 KIEs for SAM-dependent methyltransferases and proposed that the S-N motions tighten the vibrational modes of the sulfonium-methyl moiety at the S_N2 TS (18, 55, 56). Our KIE measurements together with QM modeling suggest that SET8-catalyzed methylation adopts an early, asymmetrical S_N2 mechanism with more axial compression between the methyl donor and acceptor at the TS relative to the unbound and SET8-bound ground states of SAM (Fig. 5), in agreement with previous molecular dynamics simulations (34). This motion of S-N at the TS leads to further stiffness of the vibrational modes of the C-H bonds of the methyl group. In contrast, the normal intrinsic 1°-^{13}C KIE of 1.04 is largely due to the net loss of the S-C bond order, which has not been compensated by the weak formation of the N-C bond at the early TS.

The recent elucidation of noncanonical CH–O interaction could shed light on an alternative, but mutually nonexclusive mechanism

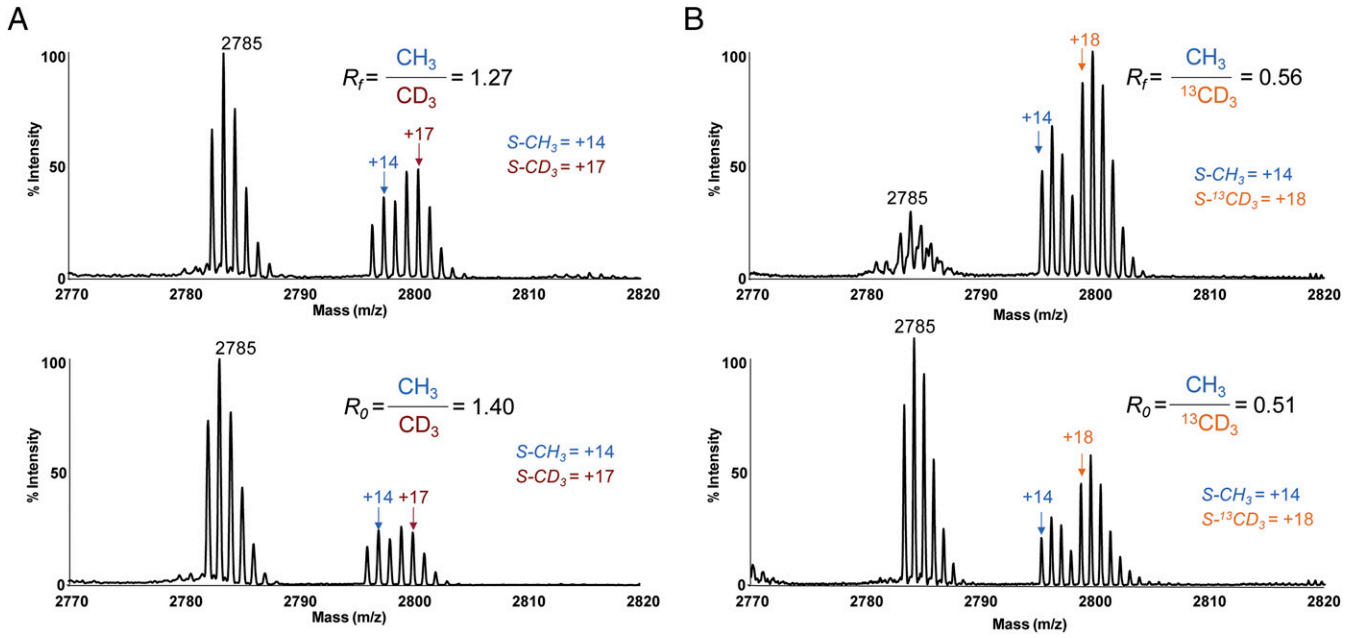

Fig. 4. (*A* and *B*) Representative MALDI-TOF-MS data for partial consumption (*Top*) and 100% consumption (*Bottom*) of (*A*) [*S*-CH_3]-SAM and [*S*-CD_3]-SAM and (*B*) [*S*-CH_3]-SeAM and [*S*-$^{13}CD_3$]-SeAM as a pair of isotopic cofactors. The ratios of [CH_3] vs. [CD_3] before initializing the reaction (R_0) and after reaching partial completion (R_f) were determined by the MS-deconvolution method (Fig. 3 and *Materials and Methods*). Their ratio R_0/R_f was used to determine the inverse KIEs according to Eq. **1**.

for the constrained TS of protein methyltransferases (36–38). In the context of the TS of SET8-catalyzed H4K20 monomethylation, the sulfonium-methyl group of SAM is expected to form three equatorial noncanonical CH–O interactions with the two backbone amide oxygens of Cys270 and Arg295 and the phenolic oxygen of the side chain of Tyr336 (Fig. S2) (57). These interactions can position the methyl group of SAM in a linear S_N2 trajectory and thus lower the energetic barrier for catalysis. These interactions may rationalize the small inverse CD_3 BIE of 0.959 and were thus corrected upon calculating intrinsic KIEs and TS structures (Eqs. **2a** and **2b**). In contrast, an inverse intrinsic α-2°-CD3 KIE ^{CD_3}k for the SAM cofactor is expected to arise from the compressed axial S-N distance at the TS. These results are consistent with the computational data of a model S_N2 transmethylation reaction, in which axial donor–acceptor compression and equatorial CH–O interaction contribute to inverse isotope effects (58).

SeAM, a SAM mimic containing a weaker methyl-chalcogen bond, showed the CD_3 BIE, forward commitment factor, and $K_{m,cofactor}$ comparable with those of SAM, as well as only a 1.94-fold difference of steady-state kinetics [$^{SeAM/SAM}(k_{cat}/K_{m,cofactor}) = 1.94$] (Table 1 and *SI Materials and Methods*). Therefore, the two cofactors may interact with SET8 in a similar manner for catalysis. Whereas SeAM has a larger intrinsic 1°-^{13}C KIE of 1.06 ± 0.02 and a small normal α-2°-CD_3 KIE of 1.02 ± 0.02 (Table 1 and *SI Materials and Methods*), computational modeling indicates that the experimental $^{^{13}CH_3}k$ and ^{CD_3}k of the SeAM-dependent H4K20 methylation match a suite of TS geometries with a relatively fixed Se-N distance around 4.9 Å but the altered position of

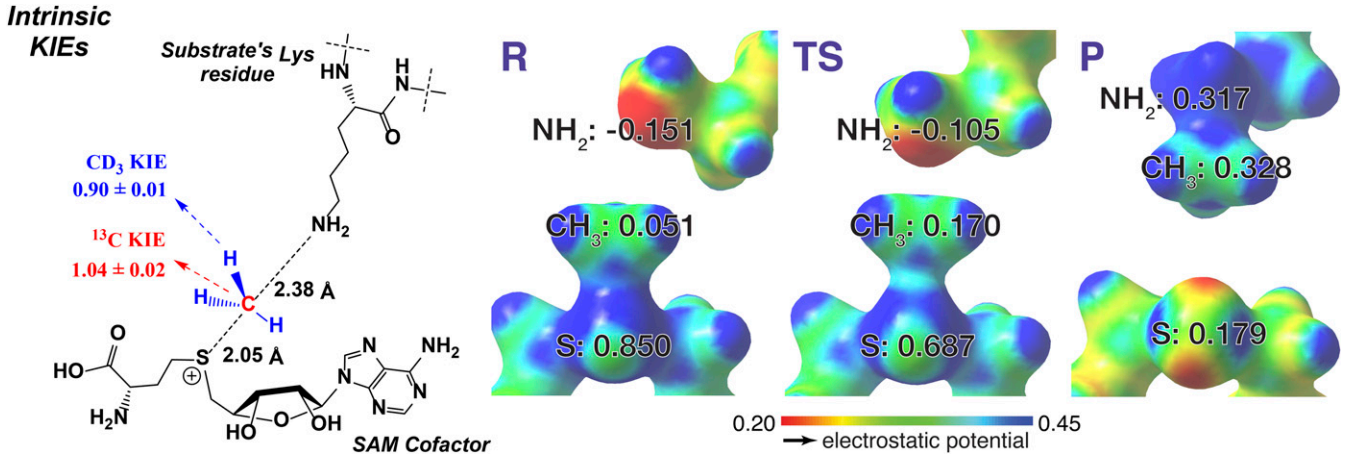

Fig. 5. TS structure of SET8-catalyzed H4K20 monomethylation with SAM as the cofactors. α-2°-CD_3 KIE and 1-^{13}C KIE (intrinsic KIEs, *Left*) were used as computational constraints to solve the TS structures. The TS (*Center*) shows an early, asymmetrical character with the long C-N and short C-S distances of 2.35–2.40 Å and 2.00–2.05 Å, respectively. The structures of reactants (R, *Left*) and products (P, *Right*) are shown for comparison. The numbers in R, TS, and P are NBO charges for S, -CH_3, and -NH_2 with red for electron rich and blue for electron deficient in ESPS maps.

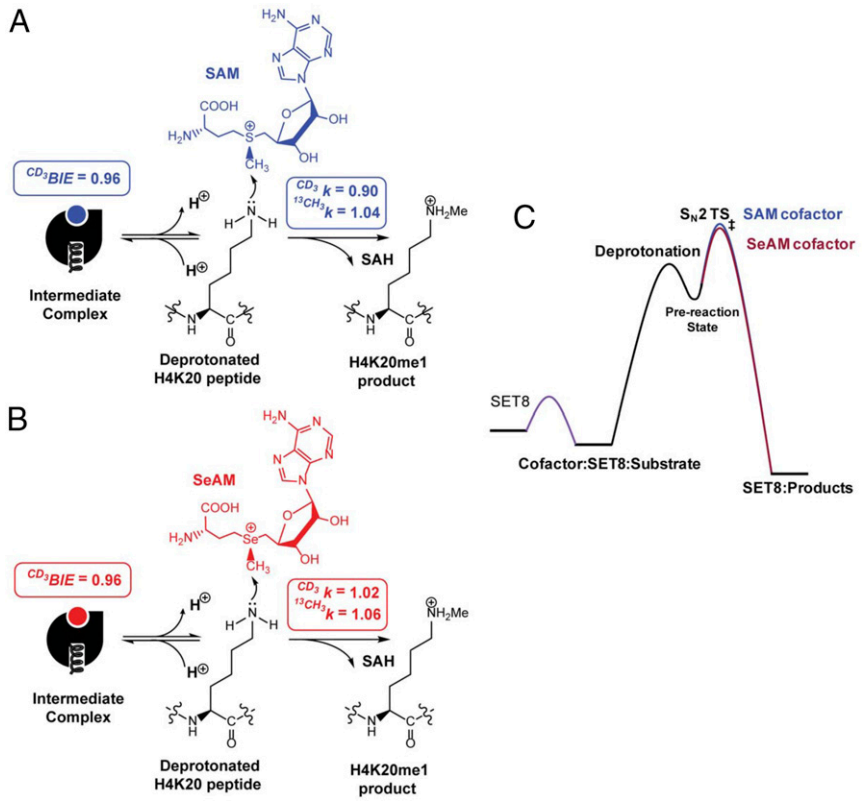

Fig. 6. Reaction path of SET8-catalyzed H4K20 monomethylation. (*A*) Reaction mechanism of SET8-catalyzed H4K20 monomethylation with the SAM cofactor. After the formation of a ternary SAM–SET8–H4K20 intermediate complex and the subsequent deprotonation, the rate-determining step of the catalysis is the formation of an early, asymmetrical S_N2 transition state for methyl transferring, reflected by an inverse CD_3 BIE of 0.96, an inverse intrinsic α-2°-CD_3 KIE of 0.90, and a normal 1°-^{13}C KIE of 1.04. (*B*) Reaction mechanism of SET8-catalyzed H4K20 monomethylation with the SeAM cofactor. The reaction path for the SeAM cofactor is similar to that for SAM with CD_3 BIE of 0.96, α-2°-CD_3 KIE of 1.02, and 1-^{13}C KIE of 1.06. (*C*) Relative energy barriers in SET8-catalyzed H4K20 monomethylation with SAM and SeAM as cofactors. SAM and SeAM are similar in terms of their affinity to SET8 and CD_3 BIE and show only 1.94-fold difference of their k_{cat} values along with the reaction path.

the methyl group between the methyl donor and acceptor (Fig. S3). We thus cannot definitively conclude the TS geometry on the basis of $^{13}CH_3k$ and ^{CD_3}k of the SeAM cofactor. The less compressed character of the SeAM-associated TS (the Se-N axial distance of 4.9 Å compared with the S-N axial distance of 4.4 Å at the TS) is consistent with the smaller magnitude of α-2°-CD_3 KIE (1.02 ± 0.02 for SeAM vs. 0.90 ± 0.01 for SAM). The longer Se-N axial distance of 4.9 Å at the TS may associate with the intrinsic chemical properties of the chalcogen atom (i.e., the slightly weaker Se-C bond with selenonium as a leaving group or the different length of the ground-state chalcogen–carbon bond of 1.95 Å for SeAM vs. 1.82 Å for SAM). Here the KIEs and BIEs of SeAM do not conflict with the early S_N2 TS of SET8-catalyzed H4K20 methylation with SAM as a cofactor.

Assembling the Reaction Pathway of SET8-Catalyzed H4K20 Monomethylation. The collective data of steady-state kinetics, CD_3 BIE, forward commitment factors, ^{CD_3}k, and $^{13}CH_3k$, as well as computational evidence, allow us to delineate SET8-mediated H4K20 methylation (Fig. 6). Along this reaction path, SET8 first binds SAM and H4K20 peptide with the apparent $K_{m,SAM}$ = 16 μM and $K_{m,peptide}$ = 40 μM to form a ternary SAM–SET8–H4K20 intermediate complex (Fig. 6 and Fig. S1). The small inverse CD_3 BIE of [*S*-CD_3]-SAM indicates that there is the equatorial CH–O interaction of the sulfonium-methyl moiety with Cys270, Arg295, and Tyr336 upon the formation of the intermediate (Fig. 6 and Fig. S2). The small forward commitment factor (C_f = 0.10) suggests a rapid exchange between unbound and SET8-bound SAM. Thereafter, the substrate is subjected to deprotonation, likely through dynamic water channels (34), to convert the positively charged ε-ammonium of the target lysine into a neutral and reactive nucleophile. The subsequent transmethylation through an early, asymmetrical S_N2 TS stands as the highest energy barrier along the reaction path (Fig. 6). At the TS, equatorial noncanonical CH–O interactions of the sulfonium-methyl hydrogens with Cys270, Arg295, and Tyr336 may further contribute to the stabilization of the TS and project readily the amine nucleophile for an S_N2 reaction as reported by the inverse ^{CD_3}k (Fig. S2). Axial compression of the methylation donor and acceptor relative to the ground state is expected at the TS. This change is accompanied by the slight loss of the net bond order of the methyl carbon at the TS as reported by the small normal $^{13}CH_3k$ (Fig. 6). SET8 is then recycled for the next turnover after releasing the methylated H4K20 and SAH as products. This observation is consistent with the early S_N2 character of the SET8-catalyzed methylation for which the TS has greater demand on the formation of the C-N bond rather than the breaking of the methyl-chalcogen bond (Fig. 5).

Comparison of TS Structures of SET8, NSD2, and Other PKMTs. PKMTs are expected to catalyze the methyl transfer from SAM to a target lysine residue of their substrates through an S_N2 mechanism. Our experimental KIEs and BIEs revealed that the SET8-catalyzed methylation goes through an early, asymmetrical S_N2 TS with the long N-C distance of 2.35–2.40 Å and the short S-C distance of 2.00–2.05 Å. Poulin et al. (59) recently reported KIEs of NSD2 and solved its TS structure. In comparison with the early S_N2 TS of SET8, the TS structure of NSD2 shows the later, asymmetrical S_N2 characters with a short N-C distance of

2.02–2.10 Å and a long S-C distance of 2.5 Å. This TS structure is reflected by a large inverse α-2°-CD_3 KIE of 0.83 and a large normal 1°-^{14}C KIE of 1.11. Their data showed that the large inverse α-2°-CD_3 KIE is mainly associated with the N-S axial compression at the TS of NSD2 because the comparable magnitude of α-2°-CD_3 KIE can be modeled regardless of the presence of active-site residues of NSD2.

Besides the TS structures of SET8 and NSD2 solved with KIEs as experimental constraints, the TS structures of the SET-domain PKMTs including SET8, the viral histone methyltransferases (vSET), Rubisco large subunit methyltransferase (LSMT), and SET7/9 have been proposed solely based on computational modeling (34, 35, 60–62). The experimentally derived TS of SET8 is consistent with previous computational TS models with the N-C and S-C distances of 2.4 Å and 2.1 Å vs. 2.5 Å and 2.0 Å, respectively (34). Among the revealed TS structures of PKMTs, SET8 shows the distinct early, asymmetrical S_N2 characters as reflected by the long N-C distance and the short S-C distance at the TS. The modeled TS structures of SET7/9 are substrate dependent with a symmetric S_N2 TS (comparable N-C and S-C distances of 2.2–2.4 Å) for histone 3 lysine 4 peptide substrate and a late, asymmetric S_N2 TS (N-C and S-C distances of 2.0 Å and 2.6 Å, respectively) for p53 lysine 372 peptide substrate (35, 60). In contrast, vSET like NSD2 adapts a late, asymmetric S_N2 TS with the N-C distance of 2.0 Å and the S-C distance of 2.6 Å; Rubisco LSMT adapts a symmetric S_N2 TS with the comparable N-C and S-C distances of 2.2–2.4 Å (59, 60). Interestingly, all of the revealed TS structures of PKMTs show a relatively fixed distance between the methyl donor and acceptor (the leaving group and nucleophile) with S-N distances around 4.4–4.6 Å but differ in the position of the methyl group (early, symmetric, or late S_N2 TS). Such a difference may present the opportunity to design selective TS analog inhibitors against PKMTs.

Materials and Methods

General Materials and Methods. Chemicals for synthesis were purchased from Sigma Aldrich and used without purification. [S-CT_3]-SAM (79.5 Ci/mmol as a fully tritiated product) and [S-$^{14}CH_3$]-SAM (58 mCi/mmol) were purchased from Perkin-Elmer. Other reagents were purchased from Fisher Scientific unless mentioned otherwise. Solvents for HPLC were degassed before use. HPLC purification of synthesized cofactors (*SI Materials and Methods*) was carried out with a Waters 600 Controller HPLC equipped with a 2,998-diode array detector and an XBridge Prep C18 5-μm OBD 19 × 150-mm reverse phase column. After collecting the desired HPLC fractions, residual solvents were removed by a Savant Sc210A SpeedVac Concentrator (Thermo), followed by lyophilization with a Flexi-Dry μP Freeze-Dryer. H4K20 peptide (residues 10–30) ([H_2N-LGKGGAKRHRKVLRDNIQGIT-GG(K-Biotin)-OH] and [H_2N-LGKGGAKRHRKVLRDNIQGIT-OH]) were prepared according to standard Fmoc-protected solid-phase peptide synthesis at the Proteomics Resource Center of Rockefeller University and purified by a reverse-phase preparative HPLC with a 0–40% acetonitrile gradient in 0.1% trifluoroacetic acid (TFA)/ddH_2O to >90% purity. The quality of the peptide was confirmed by MALDI-MS. The two H4K20 peptides were shown previously to be active substrates of SET8 with the biotinylated peptide used in the present work unless specified (63). SeAM and isotopically labeled SAM/SeAM were prepared according to previous methods (*SI Materials and Methods*).

MALDI-TOF MS. MALDI-TOF MS was implemented to quantify the ratios of isotopically labeled H4K20 peptide (CH_3- vs. CD_3- and CH_3- vs. $^{13}CD_3$- labeling), from which KIEs, BIEs, and commitment factors were obtained as detailed below. Here a mixture of SAM or SeAM and their isotopic analogs was incubated with SET8 and H4K20 peptide. After processing the reaction at ambient temperature (22 °C) for specific time intervals, the peptide sample was enriched by C18 ZipTip (Millipore), washed with 0.1% TFA/ddH_2O (vol/vol) 10 times, and eluted out with 50% acetonitrile/0.1% TFA, according to the manufacturer's instructions. The resultant peptide products were subjected to MALDI-MS as described previously (42). Briefly, to prepare MALDI-TOF-MS samples, 2 μL of the purified peptide was mixed with 1 μL of saturated α-cyano-hydroxy-cinnamic acid solution (50% acetonitrile/0.1% TFA) on a MALDI sample plate and allowed to dry at ambient temperature (22 °C). The dried samples were then subjected to MALDI-TOF-MS analysis (Voyager-DE STR; Applied Biosystems). Desorption/ionization was obtained using a delayed-extraction, positive ion mode with a 337-nm nitrogen laser (3-ns pulse width). Laser power was adjusted slightly above threshold to obtain good resolution and signal/background ratios. Spectra were gathered for at least 300 shots per position to ensure that the peak ratios were normalized over the course of data collection.

Determination of $^{CD_3}(V/K)$ and $^{13CD_3}(V/K)$ by MALDI-TOF MS. All SET8-catalyzed H4K20 methylation reactions were carried out at ambient temperature (22 °C) in the reaction buffer containing 50 mM Hepes (pH 8.5), 0.005% Tween 20, 0.0005% BSA, and 1 mM tris(2-carboxyethyl)phosphine (TCEP), unless otherwise specified. $^{CD_3}(V/K)$ was obtained with MALDI-TOF MS under internal competition conditions containing isotopic pairs of [*S*-CH_3]/[*S*-CD_3]-SAM or [*Se*-CH_3]/[*Se*-CD_3]-SAM and H4K20 peptide substrate. Individual reactions were performed in a total volume of 115 μL containing 500 nM SET8 and 20 μM H4K20 peptide substrate. For the SAM cofactor, [*S*-CH_3]-SAM and [*S*-CD_3]-SAM were premixed at a molar ratio of around 1.5:1 and then added to the reaction mixtures, resulting in around 30 μM [*S*-CH_3]-SAM and 20 μM [*S*-CD_3]-SAM, respectively (final concentrations for active isomers). The reaction mixture was split into two portions with one for 100% consumption and the other for partial consumption of 20% ~ 30% (100% and 20% ~ 30% consumption were calculated on the basis of the amount of the consumed cofactor and were obtained by quantifying modified vs. unmodified H4K20 peptide with MALDI-TOF MS). For the portion of 100% consumption, 10 μL of the mixture above was saved to quantify the ratio of [*S*-CH_3]-SAM to [*S*-CD_3]-SAM as prereacted substrates. Here, the 10-μL aliquot was diluted 10-fold with the reaction buffer to afford a 100-μL reaction mixture containing ~3 μM [*S*-CH_3]-SAM and 2 μM [*S*-CD_3]-SAM. This mixture was split into five aliquots and the consumption of [*S*-CH_3]/[*S*-CD_3]-SAM was driven to completion within 10 min by adding 10 μM SAM-free SET8 and 10 μM H4K20 peptide (the final concentrations). For the portion of 20–30% consumption, around 100 μL of the left reaction mixture was split into five aliquots. After processing the reaction to 20–30% completion within 40 min, individual aliquots were quenched by the addition of 2 μL trifluoroacetic acid. These samples were stored at –20 °C before MS analysis. For the isotopic pair of [*Se*-CH_3]/[*Se*-CD_3] cofactors, a similar protocol was used except that around 40 μM [*Se*-CH_3]-SeAM and 30 μM [*Se*-CD_3]-SeAM (final concentrations for active isomers) were used to initiate the reaction.

The ratios of the [CH_3]:[CD_3]-modified H4K20 peptide products were determined with MALDI-TOF MS as described above for the conditions of partial and 100% conversion (R_f and R_0). The ratio of the two [CH_3]:[CD_3] isotopic ratios (partial conversion R_f vs. 100% conversion R_0) afforded apparent KIEs (R_f/R_0) under the condition of the partial conversion (at least five replicates). Given that inverse KIEs were observed under these settings, KIEs on (V/K) were calculated according to Eq. **1** and used for small isotope effects, in which $^{x}(V/K)$ (x = CD_3 or $^{13}CD_3$), R_f, and R_0 are the light-to-heavy ratios at the partial and 100% completion, respectively, and f is the reacted fraction of the cofactors (~20–30% in these cases) (64). $^{13CD_3}(V/K)$ was obtained similarly as described above except that the isotopic pairs of [*S*-CH_3]/[*S*-$^{13}CD_3$]-SAM or [*Se*-CH_3]/[*Se*-$^{13}CD_3$]-SAM with the ratio around 1:1.5 were used according to the corresponding mathematic matrix (Eqs. **S3–S7**):

$$^{x}(V/K) = \frac{\log(1-f)}{\log(1-f\times R_f/R_0)}. \quad [1]$$

Forward commitment factors for SET8 with SAM and SeAM as cofactors were determined by an isotope-trapping method as described previously with slight modification (*SI Materials and Methods*) (65). The forward commitment factors C_f of SET8 with SAM or SeAM as the cofactor were obtained from the ratios (R_c) of [CD_3]-modified H4K20 peptide to [CD_3]-cofactor–bound SET8 according to $C_f = R_c/(1 - R_c)$ (11). Given that SET8-catalyzed methylation is irreversible, ^{x}k (^{CD_3}k, $^{13CD_3}k$, or $^{CT_3/^{14}CH_3}k$) was calculated on the basis of Eqs. **2a** and **2b** (66), in which $^{x}(V/K)$ [$^{CD_3}(V/K)$, $^{13CD_3}(V/K)$, or $^{CT_3/^{14}CH_3}(V/K)$] is the experimental KIE obtained via Eq. **1**, BIEs (CD_3 and CT_3 BIEs) are obtained according to Eq. **3** (the contribution of $^{13}C/^{14}C$ to BIE is expected to be negligible), and C_f is the forward commitment factor obtained via $C_f = R_c/(1 - R_c)$ (19, 64):

$$^{x}(V/K) = \frac{^{x}k \times ^{x}BIE + C_f}{1 + C_f} \quad [2a]$$

$$^{x}k = \frac{^{x}(V/K)\times(1+C_f) - C_f}{^{x}BIE}. \quad [2b]$$

Determination of BIEs by MALDI-TOF MS. To measure the CD_3 BIE of the [CH_3]:[CD_3]-cofactor pair (SAM or SeAM) with the MS-based method (Fig. 2*B*), 10 μM SET8 in the reaction buffer was incubated with a 100-μM mixture

of ~1:1 [CH_3]:[CD_3] cofactors (molar ratio) for 5 min at ambient temperature (22 °C) (110 μL as the final volume). A 10-μL portion of the mixture was saved and diluted by 10-fold with the reaction buffer. The diluted sample was mixed with 15 μM of H4K20 peptide (the final concentration) for 20 min to consume all of the cofactors. The resultant sample was subjected to MALDI-TOF MS as described above to calculate the light-to-heavy ratio of prebound [CH_3]:[CD_3] cofactors ($R_{prebound}$, five replicates). The remaining mixture (~100 μL) was subjected to a 0.5-mL PD SpinTrap G-25 (GE Healthcare) spin column (preequilibrated with the reaction buffer and maintained at 4 °C) at 800 × *g* for 1 min according to the spin protocol of the manufacturer to remove the unbound cofactors. Into the flow-through fraction of SET8-bound cofactors, 15 μM of the H4K20 peptide was added. From the reaction mixture, five aliquots were split and incubated at ambient temperature (22 °C) for 20 min to drive the reaction to completion. MALDI-TOF MS was implemented to calculate the light-to-heavy ratio of bound [CH_3]:[CD_3] cofactors (R_{bound}) according to the deconvolution method described for [CH_3]/[CD_3]-modified H4K20 peptide (*SI Materials and Methods*).

The values of BIEs were obtained on the basis of $R_{prebound}/R_{bound}$ according to Eq. **3** (67, 68), in which R_{bound} and $R_{prebound}$ are the MALDI-MS–derived light-to-heavy ratios of the bound (the samples after PD SpinTrap G-25) and prebound (the samples before PD SpinTrap G-25) cofactors, respectively; R_{free} is the light-to-heavy ratios of the unbound cofactors equilibrated with the cofactor–SET8 complex; *f* is the SET8-bound fraction of the light cofactors estimated on the basis of the concentration of SET8 and the cofactors and the K_d values of the cofactors (Eq. **S2**). The K_d values for the [CH_3]:[CD_3]-SAM and -SeAM cofactor pairs are comparable as determined below. Here apo- and cofactor-bound SET8 will be separated gradually from the unbound cofactor by the PD SpinTrap G-25 column upon centrifugation. During this process, a portion of the bound cofactor may dissociate from SET8, given the gradual depletion of the unbound cofactor pool. The resultant reequilibration of SET8-bound cofactor may increase the magnitude of BIEs in Eq. **3** if BIEs are not unity. However, such an effect is negligible because 80% ~ 90% of the estimated SET8-bound cofactors can be recovered after the centrifugation step of the PD SpinTrap G-25 column, indicating that the rate of this reequilibrium in the spin column at 4 °C is slow in comparison with the timescale for the separation of the SET8-bound cofactor vs. unbound cofactor. Here CD_3 BIE was used as $^{13}CD_3$ BIE, given the negligible contribution of ^{13}C to the binding step:

$$\mathrm{BIE} = \frac{R_{\mathrm{bound}}}{R_{\mathrm{free}}} = \frac{\frac{R_{\mathrm{bound}}}{R_{\mathrm{prebound}}} - f}{1 - f}. \qquad [3]$$

Computational Modeling and Calculation of Theoretic KIEs of SAM and SeAM. We performed theoretical TS analysis of SET8-catalyzed methyl transfer following the procedures established by the Schramm Laboratory (59, 69). The methyl transfer reaction from SAM or SeAM to a target lysine was modeled by QM simulations, using a density functional theory with an M062X functional and a 6-31+G(d,p) basis set (53). Geometry optimization and frequency calculation were performed by Gaussian09. KIEs were calculated using the ISOEFF program at the experimental temperature of 22 °C (54). The theoretical vibrational frequencies were scaled by 0.967 (70) to match experimental vibrational frequencies during KIE calculation. The structures of SAM, SeAM, and lysine were modeled as $S^+CH_3(CH_2CH_3)_2$, $Se^+CH_3(CH_2CH_3)_2$, and $CH_3CH_2NH_2$. Intrinsic KIEs of respective cofactors were obtained from experimental KIEs on (V/K) after correcting for C_f and BIEs according to Eq. **2b**. The starting atomic coordinates of the SET8-bound states of SAM and SeAM were extracted from the crystal structure of a SAM–SET8 complex (PDB 4IJ8) and optimized as local minima on the potential energy surfaces. The frequency calculations performed on the optimized structures showed no imaginary frequency.

The starting geometry of the TS was based upon the crystal structure of a SAH–SET8–H4K20me1 ternary complex (PDB ID: 2BQZ). The C-N and C-S distances were fixed at 1.6–2.5 Å and 1.9–2.8 Å with 0.1-Å increments to optimize a grid of the potential TS candidates of SET8-catalyzed H4K20 monomethylation. KIEs were predicted for these candidate TS structures and compared with experimental KIEs. The best-matched range of structures was explored with a finer grid at 0.01-Å increments in the C-N and C-S interatomic distances. Most of the constrained TS structures that matched the experimental SAM KIEs showed a small second imaginary frequency (10–20 cm^{-1}) in addition to the major imaginary frequency (100–200 cm^{-1}) that corresponds to the reaction coordinate of S–CH3–N transfer from SAM to lysine. The small second imaginary frequency is due to geometric constraints on the C-S and C-N distances and causes only marginal errors in TS predictions based on KIEs (71). The TS structures matching experimental SAM KIEs are characterized by $d_{C\text{-}S}$ = 2.00–2.05 Å and $d_{C\text{-}N}$ 2.35–2.40 Å, indicating a very early TS character for SET8-catalyzed methylation reaction. The geometry of TS without constraining the C-N and C-S distances was also calculated. The optimized TS shows a symmetric TS character with $d_{C\text{-}S}$ = 2.2 Å and $d_{C\text{-}N}$ 2.1 Å.

Similarly, the C-N and C-Se distances were fixed at 1.9–2.7 Å in and 2.1–3.0 Å with 0.1-Å increments to optimize a grid of the potential TS candidates of SET8-catalyzed H4K20 monomethylation, using SeAM as the cofactor. A range of TS structures matched experimental SeAM KIEs, as long as $d_{C\text{-}S} + d_{C\text{-}N}$ = 4.8–4.9 Å with $d_{C\text{-}S}$ of 2.2–2.7 Å and $d_{C\text{-}N}$ of 2.2–2.6 Å (Fig. S3). All those constrained TS structures had a single large imaginary frequency corresponding to Se–CH_3–N transfer.

Natural bond orbital (NBO) analysis and single-point energy calculations were then performed on the representative TS structure ($d_{C\text{-}S}$ = 2.05 Å and $d_{C\text{-}N}$ = 2.38 Å) for SAM methyl transfer, as well as the structures of corresponding reactants and products, using the NBO3.0 program available in Gaussian09. The electrostatic potential surfaces (ESPSs) were visualized in GaussView5.0 (isovalue = 0.06) from the electron density and potential cubes acquired from the checkpoint files of single-point energy calculations performed in Gaussian09.

ACKNOWLEDGMENTS. We thank Dr. V. L. Schramm and Dr. M. Poulin for scientific discussion. We thank National Institute of General Medical Sciences (Grants R01GM096056, R01GM120570, and P01GM068036), National Cancer Institute Cancer Center (Support Grant 5P30 CA008748-44), Starr Cancer Consortium, Mr. William H. Goodwin and Mrs. Alice Goodwin Commonwealth Foundation for Cancer Research, the Experimental Therapeutics Center of Memorial Sloan Kettering Cancer Center, Tri-Institutional Therapeutic Discovery Initiative, and Sohn Conference Foundation for financial support of this research.

1. Schramm VL (2011) Enzymatic transition states, transition-state analogs, dynamics, thermodynamics, and lifetimes. *Annu Rev Biochem* 80:703–732.
2. Cleland WW (2005) The use of isotope effects to determine enzyme mechanisms. *Arch Biochem Biophys* 433(1):2–12.
3. Cleland WW (1995) Isotope effects: Determination of enzyme transition state structure. *Methods Enzymol* 249:341–373.
4. Świderek K, Paneth P (2013) Binding isotope effects. *Chem Rev* 113(10):7851–7879.
5. Northrop DB (1975) Steady-state analysis of kinetic isotope effects in enzymic reactions. *Biochemistry* 14(12):2644–2651.
6. Schramm VL (2007) Binding isotope effects: Boon and bane. *Curr Opin Chem Biol* 11(5):529–536.
7. Northrop DB (2001) Uses of isotope effects in the study of enzymes. *Methods* 24(2): 117–124.
8. Li L, Luo M, Ghanem M, Taylor EA, Schramm VL (2008) Second-sphere amino acids contribute to transition-state structure in bovine purine nucleoside phosphorylase. *Biochemistry* 47(8):2577–2583.
9. Luo M, Li L, Schramm VL (2008) Remote mutations alter transition-state structure of human purine nucleoside phosphorylase. *Biochemistry* 47(8):2565–2576.
10. Schramm VL (2005) Enzymatic transition states: Thermodynamics, dynamics and analogue design. *Arch Biochem Biophys* 433(1):13–26.
11. Luo M, Singh V, Taylor EA, Schramm VL (2007) Transition-state variation in human, bovine, and Plasmodium falciparum adenosine deaminases. *J Am Chem Soc* 129(25):8008–8017.
12. Schwartz SD, Schramm VL (2009) Enzymatic transition states and dynamic motion in barrier crossing. *Nat Chem Biol* 5(8):551–558.
13. Schramm VL (2013) Transition states, analogues, and drug development. *ACS Chem Biol* 8(1):71–81.
14. Schramm VL, Horenstein BA, Kline PC (1994) Transition state analysis and inhibitor design for enzymatic reactions. *J Biol Chem* 269(28):18259–18262.
15. Bennet AJ (2012) Kinetic isotope effects for studying post-translational modifying enzymes. *Curr Opin Chem Biol* 16(5-6):472–478.
16. Chan J, Lewis AR, Gilbert M, Karwaski MF, Bennet AJ (2010) A direct NMR method for the measurement of competitive kinetic isotope effects. *Nat Chem Biol* 6(6):405–407.
17. Bates C, Kendrick Z, McDonald N, Kline PC (2006) Transition state analysis of adenosine nucleosidase from yellow lupin (Lupinus luteus). *Phytochemistry* 67(1):5–12.
18. Hegazi MF, Borchardt RT, Schowen RL (1979) alpha.-Deuterium and carbon-13 isotope effects for methyl transfer catalyzed by catechol O-methyltransferase. SN2-like transition state. *J Am Chem Soc* 101(15):4359–4365.
19. Northrop DB (1981) The expression of isotope effects on enzyme-catalyzed reactions. *Annu Rev Biochem* 50:103–131.
20. Cleland WW (1982) Use of isotope effects to elucidate enzyme mechanisms. *CRC Crit Rev Biochem* 13(4):385–428.
21. Manning KA, Sathyamoorthy B, Eletsky A, Szyperski T, Murkin AS (2012) Highly precise measurement of kinetic isotope effects using 1H-detected 2D [13C,1H]-HSQC NMR spectroscopy. *J Am Chem Soc* 134(51):20589–20592.
22. Liuni P, Olkhov-Mitsel E, Orellana A, Wilson DJ (2013) Measuring kinetic isotope effects in enzyme reactions using time-resolved electrospray mass spectrometry. *Anal Chem* 85(7):3758–3764.

23. Horenstein BA, Parkin DW, Estupiñán B, Schramm VL (1991) Transition-state analysis of nucleoside hydrolase from Crithidia fasciculata. *Biochemistry* 30(44):10788–10795.
24. Dillon SC, Zhang X, Trievel RC, Cheng X (2005) The SET-domain protein superfamily: Protein lysine methyltransferases. *Genome Biol* 6(8):227.
25. Richon VM, et al. (2011) Chemogenetic analysis of human protein methyltransferases. *Chem Biol Drug Des* 78(2):199–210.
26. Martin C, Zhang Y (2005) The diverse functions of histone lysine methylation. *Nat Rev Mol Cell Biol* 6(11):838–849.
27. Huang J, Berger SL (2008) The emerging field of dynamic lysine methylation of non-histone proteins. *Curr Opin Genet Dev* 18(2):152–158.
28. Zhang X, Wen H, Shi X (2012) Lysine methylation: Beyond histones. *Acta Biochim Biophys Sin* 44(1):14–27.
29. Kouzarides T (2007) Chromatin modifications and their function. *Cell* 128(4):693–705.
30. Varier RA, Timmers HT (2011) Histone lysine methylation and demethylation pathways in cancer. *Biochim Biophys Acta* 1815(1):75–89.
31. Greer EL, Shi Y (2012) Histone methylation: A dynamic mark in health, disease and inheritance. *Nat Rev Genet* 13(5):343–357.
32. Wu J, et al. (2011) Biochemical characterization of human SET and MYND domain-containing protein 2 methyltransferase. *Biochemistry* 50(29):6488–6497.
33. Patnaik D, et al. (2004) Substrate specificity and kinetic mechanism of mammalian G9a histone H3 methyltransferase. *J Biol Chem* 279(51):53248–53258.
34. Zhang X, Bruice TC (2008) Product specificity and mechanism of protein lysine methyltransferases: Insights from the histone lysine methyltransferase SET8. *Biochemistry* 47(25):6671–6677.
35. Zhang X, Bruice TC (2008) Mechanism of product specificity of AdoMet methylation catalyzed by lysine methyltransferases: Transcriptional factor p53 methylation by histone lysine methyltransferase SET7/9. *Biochemistry* 47(9):2743–2748.
36. Couture JF, Hauk G, Thompson MJ, Blackburn GM, Trievel RC (2006) Catalytic roles for carbon-oxygen hydrogen bonding in SET domain lysine methyltransferases. *J Biol Chem* 281(28):19280–19287.
37. Horowitz S, Yesselman JD, Al-Hashimi HM, Trievel RC (2011) Direct evidence for methyl group coordination by carbon-oxygen hydrogen bonds in the lysine methyltransferase SET7/9. *J Biol Chem* 286(21):18658–18663.
38. Horowitz S, et al. (2013) Conservation and functional importance of carbon-oxygen hydrogen bonding in AdoMet-dependent methyltransferases. *J Am Chem Soc* 135(41):15536–15548.
39. Houston SI, et al. (2008) Catalytic function of the PR-Set7 histone H4 lysine 20 monomethyltransferase is essential for mitotic entry and genomic stability. *J Biol Chem* 283(28):19478–19488.
40. Tardat M, et al. (2010) The histone H4 Lys 20 methyltransferase PR-Set7 regulates replication origins in mammalian cells. *Nat Cell Biol* 12(11):1086–1093.
41. Beck DB, Oda H, Shen SS, Reinberg D (2012) PR-Set7 and H4K20me1: At the crossroads of genome integrity, cell cycle, chromosome condensation, and transcription. *Genes Dev* 26(4):325–337.
42. Islam K, Zheng W, Yu H, Deng H, Luo M (2011) Expanding cofactor repertoire of protein lysine methyltransferase for substrate labeling. *ACS Chem Biol* 6(7):679–684.
43. Luo M (2012) Current chemical biology approaches to interrogate protein methyltransferases. *ACS Chem Biol* 7(3):443–463.
44. Ibáñez G, McBean JL, Astudillo YM, Luo M (2010) An enzyme-coupled ultrasensitive luminescence assay for protein methyltransferases. *Anal Biochem* 401(2):203–210.
45. Zheng W, et al. (2012) Sinefungin derivatives as inhibitors and structure probes of protein lysine methyltransferase SETD2. *J Am Chem Soc* 134(43):18004–18014.
46. Segel IH (1993) *Enzyme Kinetics: Behavior and Analysis of Rapid Equilibrium and Steady-State Enzyme Systems*, Wiley Classics Library Edition (Wiley, New York).
47. Bahnson BJ, Anderson VE (1991) Crotonase-catalyzed beta-elimination is concerted: A double isotope effect study. *Biochemistry* 30(24):5894–5906.
48. Anderson VE (2005) Quantifying energetic contributions to ground state destabilization. *Arch Biochem Biophys* 433(1):27–33.
49. Silva RG, Kipp DR, Schramm VL (2012) Constrained bonding environment in the Michaelis complex of Trypanosoma cruzi uridine phosphorylase. *Biochemistry* 51(34):6715–6717.
50. Bigeleisen J (1955) Statistical mechanics of isotopic systems with small quantum corrections. I. General considerations and the rule of the geometric mean. *J Chem Phys* 23(12):2264–2267.
51. Amin M, Price RC, Saunders WH (1988) Isotope effects on isotope effects - failure of the rule of the geometric mean as evidence for tunneling. *J Am Chem Soc* 110(12):4085–4086.
52. Frisch MJ, et al. (2009) *Gaussian 09* (Gaussian, Inc., Wallingford, CT).
53. Zhao Y, Truhlar DG (2008) The M06 suite of density functionals for main group thermochemistry, thermochemical kinetics, noncovalent interactions, excited states, and transition elements: Two new functionals and systematic testing of four M06-class functionals and 12 other functionals. *Theor Chem Acc* 120(1-3):215–241.
54. Anisimov V, Paneth P (1999) ISOEFF98. A program for studies of isotope effects using Hessian modifications. *J Math Chem* 26(1-3):75–86.
55. Zhang J, Klinman JP (2011) Enzymatic methyl transfer: Role of an active site residue in generating active site compaction that correlates with catalytic efficiency. *J Am Chem Soc* 133(43):17134–17137.
56. Iwig DF, Grippe AT, McIntyre TA, Booker SJ (2004) Isotope and elemental effects indicate a rate-limiting methyl transfer as the initial step in the reaction catalyzed by Escherichia coli cyclopropane fatty acid synthase. *Biochemistry* 43(42):13510–13524.
57. Couture JF, Dirk LM, Brunzelle JS, Houtz RL, Trievel RC (2008) Structural origins for the product specificity of SET domain protein methyltransferases. *Proc Natl Acad Sci USA* 105(52):20659–20664.
58. Wilson PB, Williams IH (2016) Influence of equatorial CH···O interactions on secondary kinetic isotope effects for methyl transfer. *Angew Chem Int Ed Engl* 55(9):3192–3195.
59. Poulin MB, et al. (2016) Transition state for the NSD2-catalyzed methylation of histone H3 lysine 36. *Proc Natl Acad Sci USA* 113(5):1197–1201.
60. Zhang X, Bruice TC (2008) Enzymatic mechanism and product specificity of SET-domain protein lysine methyltransferases. *Proc Natl Acad Sci USA* 105(15):5728–5732.
61. Wang S, Hu P, Zhang Y (2007) Ab initio quantum mechanical/molecular mechanical molecular dynamics simulation of enzyme catalysis: The case of histone lysine methyltransferase SET7/9. *J Phys Chem B* 111(14):3758–3764.
62. Hu P, Zhang Y (2006) Catalytic mechanism and product specificity of the histone lysine methyltransferase SET7/9: An ab initio QM/MM-FE study with multiple initial structures. *J Am Chem Soc* 128(4):1272–1278.
63. Ibanez G, et al. (2012) A high throughput scintillation proximity imaging assay for protein methyltransferases. *Comb Chem High Throughput Screen* 15(5):359–371.
64. Birck MR, Schramm VL (2004) Nucleophilic participation in the transition state for human thymidine phosphorylase. *J Am Chem Soc* 126(8):2447–2453.
65. Singh V, Lee JE, Núñez S, Howell PL, Schramm VL (2005) Transition state structure of 5′-methylthioadenosine/S-adenosylhomocysteine nucleosidase from Escherichia coli and its similarity to transition state analogues. *Biochemistry* 44(35):11647–11659.
66. Purich DL, Schramm VL (1999) *Methods in Enzymology, Enzyme Kinetics and Mechanism: Part E Energetics of Enzyme Catalysis* (Academic, New York), pp 301–355.
67. Lewis BE, Schramm VL (2003) Binding equilibrium isotope effects for glucose at the catalytic domain of human brain hexokinase. *J Am Chem Soc* 125(16):4785–4798.
68. LaReau RD, Wan W, Anderson VE (1989) Isotope effects on binding of NAD+ to lactate dehydrogenase. *Biochemistry* 28(8):3619–3624.
69. Du Q, Wang Z, Schramm VL (2016) Human DNMT1 transition state structure. *Proc Natl Acad Sci USA* 113(11):2916–2921.
70. Alecu IM, Zheng J, Zhao Y, Truhlar DG (2010) Computational thermochemistry: Scale factor databases and scale factors for vibrational frequencies obtained from electronic model chemistries. *J Chem Theory Comput* 6(9):2872–2887.
71. Hirschi JS, Takeya T, Hang C, Singleton DA (2009) Transition-state geometry measurements from (13)c isotope effects. The experimental transition state for the epoxidation of alkenes with oxaziridines. *J Am Chem Soc* 131(6):2397–2403.
72. Iwig DF, Booker SJ (2004) Insight into the polar reactivity of the onium chalcogen analogues of S-adenosyl-L-methionine. *Biochemistry* 43(42):13496–13509.
73. Bothwell IR, et al. (2012) Se-adenosyl-L-selenomethionine cofactor analogue as a reporter of protein methylation. *J Am Chem Soc* 134(36):14905–14912.
74. Blum G, Bothwell IR, Islam K, Luo M (2013) Profiling protein methylation with cofactor analog containing terminal alkyne functionality. *Curr Protoc Chem Biol* 5(1):67–88.
75. Kogami M, Koketsu M (2015) An efficient method for the synthesis of selenium modified nucleosides: Its application in the synthesis of Se-adenosyl-L-selenomethionine (SeAM). *Org Biomol Chem* 13(36):9405–9417.
76. Hoffman JL (1986) Chromatographic analysis of the chiral and covalent instability of S-adenosyl-L-methionine. *Biochemistry* 25(15):4444–4449.
77. Stecher H, et al. (2009) Biocatalytic Friedel-Crafts alkylation using non-natural cofactors. *Angew Chem Int Ed Engl* 48(50):9546–9548.
78. Dalhoff C, Lukinavicius G, Klimasăuskas S, Weinhold E (2006) Direct transfer of extended groups from synthetic cofactors by DNA methyltransferases. *Nat Chem Biol* 2(1):31–32.
79. Borchardt RT, Wu YS (1976) Potential inhibitors of S-adenosylmethionine-dependent methyltransferases. 5. Role of the asymmetric sulfonium pole in the enzymatic binding of S-adenosyl-L-methionine. *J Med Chem* 19(9):1099–1103.
80. Luo M, Schramm VL (2008) Ribosyl geometry in the transition state of Streptococcus pneumoniae methylthioadenosine nucleosidase from the 3′-(2)H kinetic isotope effect. *J Am Chem Soc* 130(35):11617–11619.
81. Luo M, Schramm VL (2008) Transition state structure of E. coli tRNA-specific adenosine deaminase. *J Am Chem Soc* 130(8):2649–2655.
82. Cook PF, Cleland WW (2007) *Enzyme Kinetics and Mechanism* (Garland Science, London).